Applied Physics Letters

Investigation of photoconductive effect on Bi_2Te_3 epitaxial film

Cite as: Appl. Phys. Lett. **114**, 112101 (2019); https://doi.org/10.1063/1.5084722
Submitted: 06 December 2018 . Accepted: 01 March 2019 . Published Online: 18 March 2019

M. J. P. Pirralho, M. L. Peres, C. I. Fornari, D. P. A. Holgado, F. S. Pena, S. Nakamatsu, P. H. O. Rappl, E. Abramof, and D. A. W. Soares

© 2019 Author(s).

Applied Physics Letters ARTICLE scitation.org/journal/apl

Investigation of photoconductive effect on Bi_2Te_3 epitaxial film

Cite as: Appl. Phys. Lett. **114**, 112101 (2019); doi: 10.1063/1.5084722
Submitted: 6 December 2018 · Accepted: 1 March 2019 ·
Published Online: 18 March 2019

View Online

Export Citation
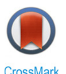
CrossMark

M. J. P. Pirralho,[1] M. L. Peres,[1,a)] C. I. Fornari,[2] D. P. A. Holgado,[1] F. S. Pena,[1] S. Nakamatsu,[1] P. H. O. Rappl,[2] E. Abramof,[2] and D. A. W. Soares[1]

AFFILIATIONS

[1]Instituto de Física e Química, Universidade Federal de Itajubá, Itajubá - MG CEP 37500-903, Brazil
[2]Laboratório Associado de Sensores e Materiais, Instituto Nacional de Pesquisas Espaciais, São José dos Campos – SP CEP 12227-010, Brazil

[a)]Author to whom correspondence should be addressed: marcelos@unifei.edu.br

ABSTRACT

In this work, we present the results of photoconductivity measurements performed in the temperature range of 12 K–300 K on a 150 nm-thick Bi_2Te_3 film grown by molecular beam epitaxy on a (111) BaF_2 substrate. A transition from negative to positive photoconductivity is found to occur around 125 K. Resistivity and Hall data measured under light and dark conditions qualitatively elucidate the observed phenomena. The Arrhenius plot of recombination times obtained from photoconductivity decay curves measured at different temperatures gives the activation energy associated with the bulk trap level. Using this activation energy as the effective trap potential, we calculated the generation and recombination rates as a function of temperature. The analysis provides a quantitative explanation that predicts the transition effect observed in the experiment. No evidence of contribution from surface states is found from the magnetoresistance curves measured at low temperatures.

Published under license by AIP Publishing. https://doi.org/10.1063/1.5084722

Bismuth telluride (Bi_2Te_3) has been widely studied over the last few decades due to its potential application in the development of thermoelectric devices.[1,2] More recently, Bi_2Te_3 has been theoretically predicted and experimentally demonstrated to be a three-dimensional topological insulator (TI), which is a new class of materials with very singular quantum-mechanical properties. Such properties are directly related to the band structure of these materials that exhibits a finite band gap in the bulk and gapless surface states with linear dispersion shaped like a Dirac cone.[3–6] In addition, Bi_2Te_3 based structures are promising candidates for application in quantum computing, spintronics, ultrafast transistors, and low-energy dissipation devices.[5,7–9] Also, near-infrared (IR) photodetectors with high performance are crucial for the photonic device development and, in addition, it is advantageous to point out that the TIs have strong optical absorbance with THz response,[4,10] and it has been demonstrated that Bi_2Te_3 TIs photodetectors can also measure the polarization state of the incident light, unlike conventional materials.[11]

It has been recently demonstrated that Bi_2Te_3 nanosheets and nanowires present broad spectral photodetection that covers from ultraviolet to near-infrared radiation, revealing the potential of this compound for the development of new photodetectors operating in this wide spectral range.[12] Moreover, the phenomenon of negative photoconductivity (NPC) has been observed in topological insulators, and it is attributed to transport via surface states. For Bi_2Te_3 polycrystalline films at room temperature, NPC has been attributed to the gap opening during illumination leading to a reduction of carrier mobility.[13] On the other hand, Bi_2Se_3 nanoflakes have presented positive photoconductivity (PPC) at higher temperatures and NPC at low temperatures ($T < 2$ K) suggesting that PPC comes from bulk contribution, while NPC originates from topological surface states.[14] The high positive photoresponse of Bi_2Se_3 nanowires fabricated using focused ion beam milling has led to enhanced broadband photodetection at room temperature.[15]

Recent work has demonstrated that the substrate temperature and the tellurium extra supply during the growth process can drastically change the electronic properties of the bulk, leading to a transition from insulator to metallic behavior accompanied by carrier type variation from *p*- to *n*-type. These characteristics interfere with the crystal quality and consequently, the defect levels.[16] However, the presence of structural defects can enhance the bulk conductivity, by adding free electrons, thereby suppressing the surface state contribution in this manner.

The Bi_2Te_3 compound has an indirect band gap of approximately 0.15 eV at room temperature,[17,18] and it crystallizes in a hexagonal

Published under license by AIP Publishing

tetradymite-type structure with its unit cell formed by three Te^1-Bi-Te^2-Bi-Te^1 quintuple layers (QLs). Inside the QLs, Bi, and Te atoms are ionically bonded, while adjacent QLs are van der Waals coupled through Te^1 atoms.[19,20] Consequently, Bi_2Te_3 is a layered material that exfoliates easily like graphite.[21] In order to develop high-quality Bi_2Te_3 devices with low noise levels, it is crucial to understand the effect of disorder on electrical transport as a function of temperature. In this work, photoconductivity measurements were performed on a Bi_2Te_3 single film using infrared (IR) light with temperatures varying from 12 K to 300 K. The results show a transition from negative to positive photoconductivity around 125 K, which is in good agreement with the simulations using the generation and recombination rates and the associated activation energy obtained from the experimental photoconduction decay curves. Magnetoresistance is also measured at different temperatures and indicates that there is no surface state contribution to the photoconductivity. The results presented in this work show a systematic way to investigate quantitatively the photoconductivity properties of Bi_2Te_3 epitaxial films and can contribute valuable information for application in sensor devices based on this compound.

For the present investigation, a Bi_2Te_3 single film was grown on a BaF_2 substrate cleaved in the (111) plane using an MBE Riber 32 system charged with a nominal stoichiometric Bi_2Te_3 solid source. Details about the MBE growth and the structural properties of the film are published elsewhere.[22,23] The substrate temperature was kept constant at 260 °C, and a beam equivalent pressure of 5.1×10^{-7} Torr was used for the Bi_2Te_3 source. A film thickness of 150 nm is achieved after 2 h of growth. A sample piece of $3 \times 3\,mm^2$ was prepared in the van der Pauw geometry by soldering four gold wires with indium pellets. The sample is mounted on a DE-202 closed He cryostat system from ARS Inc. Resistivity and Hall effect measurements were performed using a Keithley 80A system, assembled together with a Walker Scientific HV4 magnet up to 0.72 T and a PID Lakeshore 303 temperature controller. For photoconductivity measurements, an infrared LED with a peak wavelength of 930 nm was mounted in front of the sample, and the curves were recorded with an optical power density of 12 mW/m^2. The inset in Fig. 1(a) shows a schematic diagram of the sample assembly for the photoconductivity measurements. The magnetoresistance (MR) was measured using a Physical Property Measurement System from Quantum Design composed of a He-cooled superconducting system with a magnetic field up to 9 T. Measurements always started from minimum temperatures, which are 12 K for photoconductivity and 1.9 K for magnetoresistance.

Figure 1(a) shows the photoconductivity curves, normalized to the value under dark conditions just before illumination at t = 0 (σ_0), measured on the Bi_2Te_3 film for temperatures between 12 K and 300 K. At high temperatures, a square-shaped negative photoconductivity is observed for this sample, with fast saturation when light is on and fast decay after illumination is removed. As temperature decreases, the Bi_2Te_3 film undergoes a transition in which the photoconductivity becomes positive at temperatures below 125 K, approximately. Also, the photoconductivity curves in this temperature region have profiles completely different from those at $T > 125$ K, and it is clear that the sample presents a strong persistent photoconductive effect (PPC) when illumination is removed, i.e., the conductivity value before illumination is not restored to its original value under dark conditions. This is mainly caused by defect states that introduce energy levels within the energy band gap that can act as trap levels depending on the temperature region.

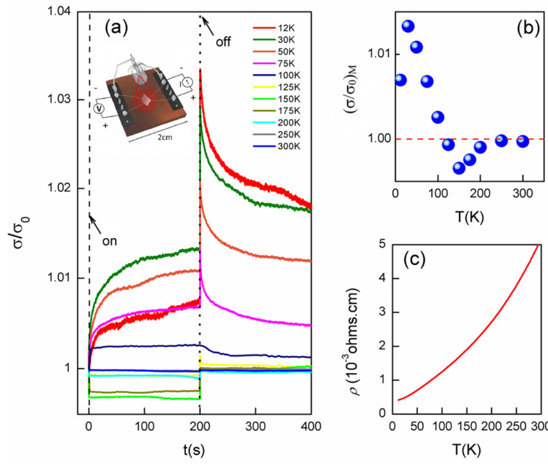

FIG. 1. (a) Photoconductivity curves normalized to the value just before illumination at t = 0 (σ_0) of the Bi_2Te_3 film measured at temperatures from 12 K to 300 K. The dashed (dotted) line indicates the time when the light is turned on (off). Inset: Schematic representeation of sample set up. (b) Temperature dependence of the maximum values of normalized photoconductivity $(\sigma/\sigma_0)_M$ measured under illumination at t = 200 s just before the light is switched off. (c) Electrical resistivity (ρ) as a function of temperature.

In addition, in the positive photoconductivity region, there are well-pronounced peaks in the curves when light is removed [see the dotted line in the graph of Fig. 1(a)] that can be attributed to the ceasing of photogeneration rate. Since defect states are no longer photoionized, the recombination rate from the conduction band to the defect levels is reduced, instantly inducing the observed photoconductivity peaks.[24–26] Figure 1(b) shows the values of the maximum amplitude of curves presented in Fig. 1(a), when sample is under illumination (at t = 200 s) just before illumination is switched off. In this figure, the maximum normalized photoconductivity amplitude $[(\sigma/\sigma_0)_M]$ is very close to one at 300 K and 250 K and starts to exhibit increasing negative amplitude $[(\sigma/\sigma_0)_M < 1]$ at temperatures of 200, 175, and 150 K. This behavior changes around 150 K and at temperatures lower than 125 K, the amplitude presents increasing positive photoconductivity, as described before. From these curves, one also observes that the photoresponse is very small, around 1%. This is due to the metallic character of the sample. Figure 1(c) shows the electrical resistivity (ρ) as a function of temperature, indicating the metallic behavior in the whole range of temperatures. The small value of ρ indicates that the sample is highly degenerated,[27] and hence photogenerated carriers are less effective than in the case of insulating samples.

Electrical transport parameters were obtained using Hall effect measurements under light and dark conditions to investigate the transition observed in Fig. 1(a). Figure 2(a) shows the carrier concentration (n) under light (on) and dark conditions (off). There is almost no difference between the curves when the temperature decreases from 300 K down to 150 K. For temperatures below 150 K, the curve under illumination has higher values than the curve under dark conditions, leading to the positive contribution to photoconductivity. Figure 2(c) shows the difference between carrier concentration values under light and dark conditions as $\Delta n(T) = (n^{on}(T) - n^{off}(T))/n^{on}(T)$, showing the percentage contribution to positive photoconductivity. Between 150 K and 300 K, the curve oscillates, exhibiting regions of negative contribution (see arrow).

Published under license by AIP Publishing

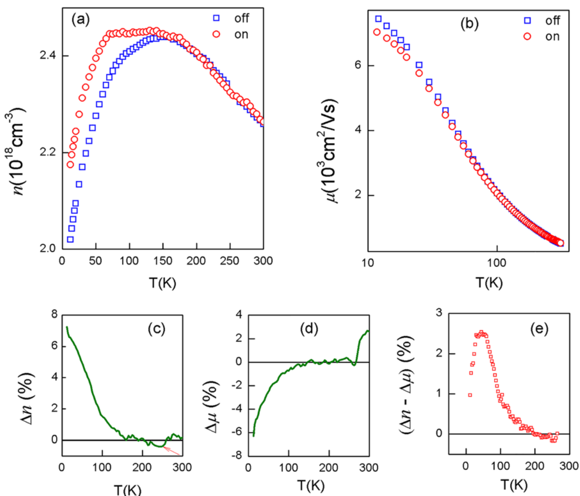

FIG. 2. (a) Carrier concentration and (b) mobility under light (red open circles) and dark (blue open squares) conditions, as obtained by Hall measurements. Percentage difference between the values under light and dark conditions of (c) carrier concentration $\Delta n(T) = (n^{on}(T) - n^{off}(T))/n^{on}(T)$, evidencing the contribution to positive photoconductivity, and of (d) carrier mobility $\Delta\mu(T) = (\mu^{on}(T) - \mu^{off}(T))/\mu^{on}(T)$, giving negative contribution to photoconductivity. (e) Difference $\Delta n(T) - \Delta\mu(T)$ that gives the total contribution.

Below 150 K, the positive contribution is clear and increases as temperature decreases. Figure 2(b) presents the carrier mobility under light and dark conditions. In this case, the carrier mobility under illumination is lower than the values under dark conditions at lower temperatures, giving negative contribution to photoconductivity. At higher temperatures, the difference between the curves is not perceptible. Figure 2(d) shows the calculated percentage difference between carrier mobility under light and dark conditions shown in Fig. 2(b), $\Delta\mu(T) = (\mu^{on}(T) - \mu^{off}(T))/\mu^{on}(T)$, where the negative contribution to photoconductivity is clear and appears to be more effective below 150 K.

According to these observations, there is a competition between the positive and negative contributions to the photoconductivity stemming from electron concentration and mobility, respectively. To verify the temperature region where each contribution is most effective, we present the percentage difference, $\Delta n(T) - \Delta\mu(T)$, in Fig. 2(e). In this figure, it can be observed that for temperatures in the range 200 K–300 K, the total contribution tends to be negative, although the amplitude is very small. For temperatures below 200 K, the positive contribution predominates. The profile shown in this figure is very similar to that in Fig. 1(b). This analysis provides only a qualitative explanation about the transition observed in the photoconductivity curves presented in Figs. 1(a) and 1(b) and the drop around 50 K in Fig. 2(e) is not observed in Fig. 1(a). This indicates that an additional mechanism could be present in the photoconductive effect that cannot be fully described by Hall analysis.

It is possible to obtain a deeper understanding of the PPC effect by analyzing the decay curves of the photoconductivity profiles when illumination is removed, as shown in Fig. 1(a). In such analysis, we consider that the defect level existence may be responsible for the anomalous characteristics observed in the photoconductivity. Such defect levels could alter significantly the carrier recombination times depending on the energy of the defect level (activation energy). It is possible to extract the recombination time according to the relation $\sigma(t) = \sigma_0 \exp\left(-\frac{t}{\tau}\right)$, where σ_0 is the conductivity under dark conditions and τ is the recombination time related to the activation energy (ε_a) through the relation $\tau = \tau_0 e^{\varepsilon_a/k_B T}$, where k_B is the Boltzmann constant.[27]

As an example, the photoconductivity data at 12 K (open circles) measured after the LED is turned off are presented in Fig. 3(a) together with the fitted curve (solid line) using the exponential decay relation, from which the recombination time can be extracted. Table I displays the recombination times obtained from these fittings at different temperatures and the respective Arrhenius plot is shown in Fig. 3(b). An activation energy of $\varepsilon_a = (37\pm5)$ meV is obtained from the linear fitting [dashed line in Fig. 3(b)].

A quantitative analysis of the photoconductivity transition effect can be obtained by deriving the generation and recombination rates and observing their temperature dependence. For this analysis, we consider the influence of the effective potential, E_t, according to the expressions[28]

$$r_{tv} = p n_d v S_p, \tag{1}$$

$$r_{ct} = n(N - n_d) v S_n, \tag{2}$$

$$g_{vt} = (N - n_d) N_v v S_p \exp\left(-\frac{E_g - E_t}{k_B T}\right), \tag{3}$$

$$g_{tc} = n_d N_c v S_n \exp\left(-\frac{E_t}{k_B T}\right), \tag{4}$$

where r_{tv} is the recombination rate from the level E_t to the valence band, r_{ct} is the recombination rate from the conduction band to the level E_t, g_{vt} is the generation rate from the valence band to the level E_t and g_{tc} is the generation rate from level E_t to the conduction band, n_d is the density of states occupied by electrons, v is the thermal velocity

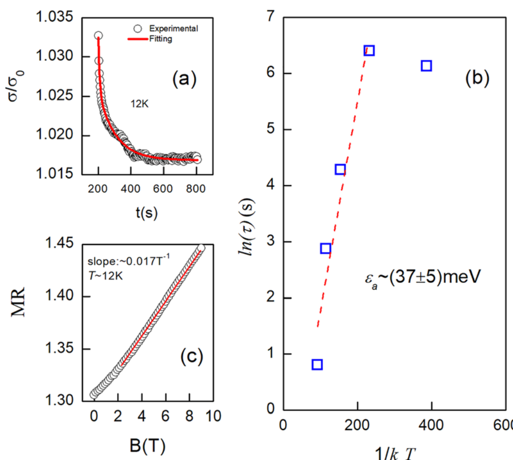

FIG. 3. (a) Photoconductivity data at 12 K (open circles) measured after light is turned off together with the fitted curve (solid line) using the exponential decay expression. The recombination time is extracted from this fitting. (b) Arrhenius plot of recombination times obtained from photoconductivity decay at different temperatures. The linear fit (dashed line) gives the activation energy ε_a. (c) Magnetoresistance curve at $T \sim 12$ K with the magnetic field swept up to 9 T (open circles) and a linear fit (straight red line).

Published under license by AIP Publishing

TABLE I. Recombination time τ obtained from exponential fittings at different temperatures.

T (K)	$(\tau \pm 0.1)$s
12	121
30	458
50	599
75	72
100	17
125	2

of free carriers, S_p and S_n are the cross-sections of holes and electrons, respectively, and N_c and N_v are the effective densities of states in the conduction and valence bands, respectively, and N is the total number of defects.

One can extract N from magnetoresistance (MR) measurements. For disordered systems, MR can exhibit linear behavior instead of the classical parabolic behavior.[29] According to the model, MR will behave linearly with B following the expression $[\rho(B,T) - \rho(0,T)]/\rho(0,T) = NB/\pi n^2 e\rho(0,T)$, where $\rho(B,T)$ is the electrical resistivity as functions of magnetic field and temperature. Hence, from the slope of the MR curve, one can extract the value of N. Figure 3(c) shows the linear fitting, with a slope of $\sim$0.017 T^{-1} at 12 K. This gives $N \sim 4 \times 10^{23}$ m^{-3}, where we used $\rho(0,T) \sim 0.5 \times 10^{-5}\,\Omega$ m and $n \sim 2.2 \times 10^{24}$ m^{-3} from Hall data. The number of occupied defect states can be calculated as $n_d = f_e N$, where $f_e = 1/\{e^{[\varepsilon_i - \varepsilon_F(x)]/k_B T} + 1\}$ is the Fermi-Dirac distribution, where ε_i assumes the value of 37 meV. For the Fermi energy, we use the parabolic approximation, $\varepsilon_F(x) = \hbar^2 k_F^2/2m^*$, where m^* is the effective mass $\sim$0.178 m_e[30] and $k_F = (3\pi^2 n)^{1/3}$. We also considered that S_p and S_n have approximately the same value. If there is 20% difference between S_p and S_n, for example, this would give a difference of only 4% in the values of the obtained curves.

The total contribution for positive photoconductivity is $(g_{vt} + g_{tc})$, which increases the carrier density in the valence and conduction bands. On the other hand, the total contribution to negative photoconductivity is $(r_{tv} + r_{ct})$ that indicates the decrease of carrier in the valence and conduction bands. Hence, we calculate the ratio $(g_{vt} + g_{tc})/(r_{tv} + r_{ct})$ as a function of temperature whose behavior is shown in Fig. 4(a). In this figure, we observe that as temperature decreases from 300 K down to about 225 K, the ratio presents values smaller than 1, indicating that negative photoconductivity must be present in the measurements. Further decrease in temperature leads to an increase in the ratio, which becomes greater than 1 at $T \sim 126$ K, and therefore, for $T < 126$ K, positive photoconductivity must dominate. The inset in Fig. 4(a) presents a diagram that represents the generation and recombination processes. For $T < 126$ K, the generation rates g_{vt} and g_{tc} are more effective, leading to an increase in electrons and holes in the conduction and valence bands, respectively. On the other hand, for $T > 126$ K, the recombination r_{tv} and r_{ct} dominates, leading to a decrease in free carriers. These predictions are in very good agreement with the transition in photoconductivity observed here for Bi_2Te_3 [Figs. 1(a) and 1(b)] at $T \sim 125$ K, which can be explained by the influence of a total energy barrier that act as a trap to carriers.

Finally, regarding the topological nature of Bi_2Te_3, it is also possible that the contribution to transport via surface states could lead to

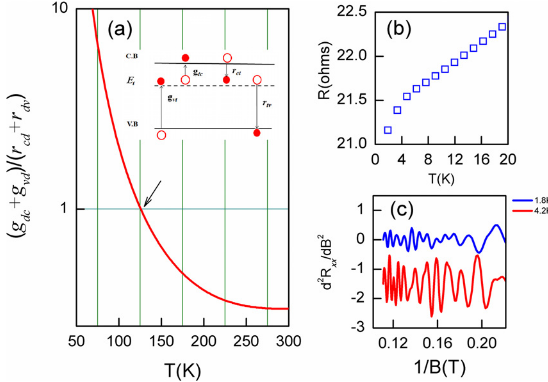

FIG. 4. (a) Ratio of generation and recombination rates $(g_{vt} + g_{tc})/(r_{tv} + r_{ct})$, calculated as a function of temperature. Ratio values smaller (higher) than one indicates that negative (positive) photoconductivity dominates. The inset shows an energy diagram of the generation and recombination processes. (b) Electrical resistance R as a function of temperature in the range of 1.8 K–20 K. (c) Second derivative of R_{xx} with respect to B as function of 1/B at temperatures of 1.8 K and 4.2 K.

the effects observed in the photoconductivity in this sample. In this case, if the surface channel is effectively contributing to the transport, the photoresponse would be a combination of transitions in the bulk and surface states of the Bi_2Te_3[7] film. Such contribution would become more effective in the temperature region where the transition from negative to positive photoconductivity is observed, as shown in Fig. 1. In order to verify this scenario, we plot in Fig. 4(b) the electrical resistance R as a function of temperature in the range of 1.8 K–20 K. The sample resistance decreases as temperature decreases, following the metallic behavior for degenerate semiconductors. For temperatures below 4 K, approximately, we observe a slight drop in R. This could indicate the presence of a weak antilocalization effect or just the reduction of phonon scattering. In the case of weak antilocalization, spin-orbit coupling is an indication that surface states could be contributing significantly to transport.[31] In the case of surface states, Shubnikov–de Haas oscillations should be present, and hence we performed magnetoresistance measurements at 1.8 K and 4.2 K. The second derivative was applied to remove the background contribution, and the resulting curves are presented in Fig. 4(c) as a function of 1/B. In fact, some oscillations can be detected, but no periodic pattern in 1/B is evident. Also, the amplitude of oscillations is smaller at lower temperatures, which is the opposite of the expected quantum behavior where Landau levels sweep the Fermi level. Therefore, we conclude that the effects observed in the presented photoconductivity measurements originate mostly from generation and recombination rates that are significantly affected by temperature variation, as demonstrated quantitatively by the theoretical model.

Several publications on photoconductivity and magnetotransport measurements performed on nanofabricated bismuth chalcogenide devices indicate that the topological surface states are responsible for the observed effects. The modulation of surface states using gate voltages on a series of Bi_2Te_3 nanoribbons with different dimensions was investigated.[32] They showed that samples with large surface-to-volume ratios enhance surface conductivity. Magnetoresistance oscillations performed at low temperatures ($\sim$1.4 K) showed strong evidence of surface transport with applied positive gate voltages. Recent

Published under license by AIP Publishing

measurements of photoconductive effects on Bi_2Te_3 nanosheets and nanowires[12] and on Bi_2Se_3 nanoflakes[14] and nanowires[15] were attributed to the conduction via topological surface states, mainly due to the large surface-to-volume ratio in these nanodevices. Also, Shubnikov–de Haas oscillations and Aharonov–Bohm interference effects measured on Bi_2Se_3 nanowires fabricated by focused ion beam milling[33,34] were considered as a manifestation of robust topological surface states in nanostructures of this TI material. Moreover, the robustness of surface states against disorder was demonstrated by the measurement of magnetoconductance oscillations at low temperatures (1.8 K) on Bi_2Te_3 nanotubes.[35] Contrarily, our temperature dependent photoconductivity measurements on a 150 nm-thick Bi_2Te_3 film point to bulk conduction through a trap level, and the phenomenon is well explained by a generation and recombination theoretical model. The much smaller surface-to-volume ratio in our film may be responsible for the difference between our results and the ones obtained for the nanodevices. It is important to mention that recent publications in the magnetotransport of Bi_2Te_3 thin films (see Ref. 36 and some references therein) concluded that the observed Shubnikov–de Haas oscillations come from the bulk cylindrical Fermi surface of Bi_2Te_3. In this case, the angle dependence of the bulk magnetoresistance oscillations is two-dimensional in nature (not due to the surface states but due to anisotropic bulk transport). Therefore, by comparing the results of all these works, one can conclude that the conductance through topological surface states in Bi_2Te_3 thin films is still controversial.

In this work, we presented photoconductivity measurements using infrared illumination on a 150 nm-thick Bi_2Te_3 film grown by MBE technique on a (111) BaF_2 substrate. A transition from negative to positive photoconductivity was found to occur around 125 K. The transition effect was analyzed using the recombination and generation equations, and the associated activation energy, calculated from the recombination time, obtained from the experimental photoconduction decay curves. From this analysis, we found the existence of a potential barrier of (37 ± 5) meV associated with a defect level inside the band gap of the material. Thus, we showed that the transition is caused by the defect states within the band structure that act as traps for the carriers, altering the recombination and generation rates as temperature varies. We also investigated the magnetoresistance curves and found no evidence of contribution from surface states. The systematic analysis presented in this work allows a better understanding of the role of defects in the photoconductive effect observed in Bi_2Te_3 thin films.

We would like to thank CAPES, CNPq (No. 307933/2013) and FAPEMIG (No. APQ-00623-14) for financial support.

REFERENCES

[1] J. P. Heremans, V. Jovovic, S. T. Eric, A. Saramat, K. Kurosaki, A. Charoenphakdee, S. Yamanaka, and J. G. Snyder, Science **321**, 554–557 (2008).
[2] S. K. Mishrayz, S. Satpathyyz, and O. J. Jepsen, Phys.: Condens. Matter **9**, 461–470 (1997).
[3] Y. Li, G. Wang, X. G. Zhu, M. H. Liu, C. Ye, X. Chen, Y. Y. Wang, K. He, L. L. Wang, X. C. Ma, H. J. Zhang, X. Dai, Z. Fang, X. C. Xie, Y. Liu, X. L. Qi, J. F. Jia, S. C. Zhang, and Q. K. Xue, Adv. Mater. **22**, 4002–4007 (2010).
[4] H. Zhang, C. X. Liu, X. L. Qi, X. Dai, Z. Fang, and S. C. Zhang, Nat. Phys. **5**, 438–442 (2009).
[5] Y. L. Chen, J. G. Analytis, J.-H. Chu, Z. K. Liu, S.-K. Mo, X. L. Qi, H. J. Zhang, D. H. Lu, X. Dai, Z. Fang, S. C. Zhang, I. R. Fisher, Z. Hussain, and Z.-X. Shen, Science **325**, 178–181 (2009).
[6] D. Hsieh, Y. Xia1, D. Qian, L. Wray, J. H. Dil, F. Meier, J. Osterwalder, L. Patthey, J. G. Checkelsky, N. P. Ong, A. V. Fedorov, H. Lin, A. Bansil, D. Grauer, Y. S. Hor, R. J. Cava, and M. Z. Hasan, Nat. Lett. **460**, 1101–1105 (2009).
[7] J. Liu, Y. Li, Y. Song, Y. Ma, Q. Chen, Z. Zhu, L. Pengfei, and S. Wang, Appl. Phys. Lett. **110**, 141109 (2017).
[8] J.-P. Xu, M.-X. Wang, Z. L. Liu, J.-F. Ge, X. Yang, C. Liu, Z. A. Xu, D. Guan, C. L. Gao, D. Qian, Y. Liu, Q.-H. Wang, F.-C. Zhang, Q.-K. Xue, and J.-F. Jia, Phys. Rev. Lett. **114**, 017001 (2015).
[9] V. Iyer, Y. P. Chen, and X. Xu, Phys. Rev. Lett **121**, 026807 (2018).
[10] P. Seifert, K. Vaklinova, K. Kern, M. Burghard, and A. Holleitner, Nano Lett. **17**, 973–979 (2017).
[11] J. D. Yao, J. M. Shao, S. W. Li, D. H. Bao, and G. W. Yang, Sci. Rep. **5**, 14184 (2015).
[12] A. Sharma, A. K. Srivastava, T. D. Senguttuvan, and S. Husale, Sci. Rep. **7**, 17911 (2017).
[13] H. Zhang, J. Yao, J. Shao, H. Li, S. Li, D. Bao, C. Wang, and G. Yang, Sci. Rep. **4**, 5876 (2014).
[14] B. Bhattacharyya, A. Gupta, T. D. Senguttuvan, V. N. Ojha, and S. Husale, Phys. Status Solidi B **255**, 800340 (2018).
[15] A. Sharma, B. Bhattacharyya, A. K. Srivastava, T. D. Senguttuvan, and S. Husale, Sci. Rep. **6**, 19138 (2016).
[16] C. I. Fornari, P. H. O. Rappl, S. L. Morelhão, G. Fornari, J. S. Travelho, S. Castro, M. J. P. Pirralho, F. S. Pena, M. L. Peres, and E. Abramof, Mater. Res. Express **5**, 116410 (2018).
[17] G. A. Thomas, D. H. Rapkine, R. B. Van Dover, L. F. Mattheiss, W. A. Sunder, L. F. Schneemeyer, and J. V. Waszczak, Phys. Rev. B **46**, 1553–1556 (1992).
[18] D. L. Greenaway and G. Harbere, J. Phys. Chem. Solids **26**, 1585–1604 (1965).
[19] X. Li, H. Ren, and Y. Luo, Appl. Phys. Lett. **98**, 083113 (2011).
[20] D. L. Medlin, Q. M. Ramasse, C. D. Spataru, and N. Y. C. Yang, J. Appl. Phys. **108**, 043517 (2010).
[21] J. Krumrain, G. Mussler, S. Borisova, T. Stoica, L. Plucinski, C. M. Schneider, and D. Grutzmacher, J. Cryst. Growth **324**, 115–118 (2011).
[22] C. I. Fornari, P. H. O. Rappl, S. L. Morelhão, and E. Abramof, J. Appl. Phys. **119**, 165303 (2016).
[23] C. I. Fornari, P. H. O. Rappl, S. L. Morelhão, T. R. F. Peixoto, H. Bentmann, F. Reinert, and E. Abramof, APL Mater. **4**, 106107 (2016).
[24] M. J. P. Pirralho, M. L. Peres, D. A. W. Soares, P. C. O. Braga, F. S. Pena, C. I. Fornari, P. H. O. Rappl, and E. Abramof, Phys. Rev. B **95**, 075202 (2017).
[25] P. C. Wei, S. Chattopadhyay, M. D. Yang, S. C. Tong, J. L. Shen, C. Y. Lu, H. C. Shih, L. C. Chen, and K. H. Chen, Phys. Rev. B **81**, 045306 (2010).
[26] R. Sreekumar, R. Jayakrishnan, C. S. Kartha, and K. P. Vijayakumar, J. Appl. Phys. **100**, 033707 (2006).
[27] M. A. B. Tavares, M. J. da Silva, M. L. Peres, S. de Castro, D. A. W. Soares, A. K. Okazaki, C. I. Fornari, P. H. O. Rappl, and E. Abramof, Appl. Phys. Lett. **110**, 042102 (2017).
[28] K. Lischka, R. Durstberger, G. Lindemann, and H. Stauding, Phys. Status Solidi B **123**, 319 (1984).
[29] A. A. Abrikosov, Phys. Rev. B **58**, 2788 (1998).
[30] B. Y. Yavorsky, N. F. Hinsche, I. Mertig, and P. Zahn, Phys. Rev. B **84**, 165208 (2011).
[31] J. Chen, H. J. Qin, F. Yang, J. Liu, T. Guan, F. M. Qu, G. H. Zhang, J. R. Shi, X. C. Xie, C. L. Yang, K. H. Wu, Y. Q. Li, and L. Lu, Phys. Rev. Lett. **105**, 176602 (2010).
[32] F. Xiu, L. He, Y. Wang, L. Cheng, L.-T. Chang, M. Lang, G. Huang, X. Kou, Y. Zhou, X. Jiang, Z. Chen, J. Zou, A. Shailos, and K. L. Wang, Nat. Nanotechnol. **6**, 216 (2011).
[33] B. Bhattacharyy, A. Sharma, V. P. S. Awana, T. D. Senguttuvan, and S. Husale, J. Phys.: Condens. Matter **29**, 07LT01 (2017).
[34] B. Bhattacharyy, A. Sharma, V. P. S. Awana, A. K. Srivastava, T. D. Senguttuvan, and S. Husale, J. Phys.: Condens. Matter **29**, 115602 (2017).
[35] R. Du, H. Hsu, A. C. Balram, Y. Yin, S. Dong, W. Dai, W. Zhao, D. Kim, S. Yu, J. Wang, X. Li, S. E. Mohney, S. Tadigadapa, N. Samarth, M. H. W. Chan, J. K. Jain, C. Liu, and Q. Li, Phys. Rev. B **93**, 195402 (2016).
[36] P. Ngabonziza, Y. Wang, and A. Brinkman, Phys. Rev. Mater. **2**, 044204 (2018).

Published under license by AIP Publishing